Effects of power per pulse on reactive HiPIMS deposition of ZrO_2 films: A time-resolved optical emission spectroscopy study

Andrea D. Pajdarová, and Jaroslav Vlček

Citation: Journal of Vacuum Science & Technology A **37**, 061305 (2019); doi: 10.1116/1.5125721
View online: https://doi.org/10.1116/1.5125721
View Table of Contents: https://avs.scitation.org/toc/jva/37/6
Published by the American Vacuum Society

HIDEN ANALYTICAL
Instruments for Advanced Science
Contact Hiden Analytical for further details:
W www.HidenAnalytical.com
E info@hiden.co.uk
CLICK TO VIEW our product catalogue

Gas Analysis
- dynamic measurement of reaction gas streams
- catalysis and thermal analysis
- molecular beam studies
- dissolved species probes
- fermentation, environmental and ecological studies

Surface Science
- UHV TPD
- SIMS
- end point detection in ion beam etch
- elemental imaging - surface mapping

Plasma Diagnostics
- plasma source characterization
- etch and deposition process reaction kinetic studies
- analysis of neutral and radical species

Vacuum Analysis
- partial pressure measurement and control of process gases
- reactive sputter process control
- vacuum diagnostics
- vacuum coating process monitoring

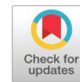

Effects of power per pulse on reactive HiPIMS deposition of ZrO_2 films: A time-resolved optical emission spectroscopy study

Andrea D. Pajdarová and Jaroslav Vlček[a)]
Department of Physics and NTIS—European Centre of Excellence, University of West Bohemia, Univerzitní 8, Plzeň 306 14, Czech Republic

(Received 26 August 2019; accepted 6 November 2019; published 19 November 2019)

Time-resolved optical emission spectroscopy was carried out during controlled reactive high-power impulse magnetron sputtering of ZrO_2 films in argon–oxygen gas mixtures. The effects of increased target power density (up to $3.0\,kW\,cm^{-2}$) applied in voltage pulses shortened from 200 to $50\,\mu s$ were studied at a nearly constant deposition-averaged target power density (close to $50\,W\,cm^{-2}$) and a fixed repetition frequency of 500 Hz. The trends in time evolution of the local ground-state densities of Zr, Ar, and O atoms and that of the Zr^+, Zr^{2+}, Ar^+, and O^+ ions during a voltage pulse were deduced from the time evolution of the corresponding excited-state populations and the excitation temperature. It was found that the sputtered Zr atoms are much more ionized (with a high fraction of Zr^{2+} ions) and the Ar atom density is more decreased near the target during the shorter ($50\,\mu s$) high-power pulses. These shorter pulses produce a four times higher pulse-averaged target power density oscillating between 1.7 and $2.1\,kW\,cm^{-2}$ during deposition. Under these conditions, much higher densities of O atoms and Zr^{2+} ions were measured in the plasma bulk. The higher backward flux of the Zr^+ and Zr^{2+} ions onto the target during this high-power discharge regime contributed significantly to a 34% decrease in the efficiency of the magnetron sputter deposition of ZrO_2 films. *Published by the AVS.* https://doi.org/10.1116/1.5125721

I. INTRODUCTION

At present, high-power impulse magnetron sputtering (HiPIMS) discharges are used in the reactive sputter deposition of oxide, nitride, and oxynitride films (see, for example, Refs. 1–4 and the works cited therein). However, the reactive HiPIMS deposition of dielectric films faces serious problems, exhibiting low deposition rates and arcing on target surfaces at high target power densities (up to several $kW\,cm^{-2}$). This arcing is especially problematic for voltage pulses longer than approximately $40\,\mu s$.

A pulsed reactive gas flow control (RGFC) has been proposed[5] to overcome the limitations of reactive HiPIMS deposition. This simple feedback control can be used in conjunction with a to-substrate reactive gas injection into the high-density plasma in front of the sputtered target. Together, this makes it possible to deliver a high power into the discharge pulses without arcing on the target. Also, this makes it possible to maintain a sputter deposition of stoichiometric films in a region close to the metallic mode. Therefore, the controlled reactive HiPIMS can be used for high-rate depositions of densified dielectric stoichiometric films.[5–7]

In our recent paper,[8] we presented a methodology for monitoring trends in the ground-state densities of particles near the sputtered target and in the plasma bulk using optical emission spectra. This methodology was used to describe the processes on the target surface and in a discharge plasma during reactive HiPIMS deposition of ZrO_2 films. This deposition was controlled by an RGFC system at the deposition-averaged target power density of $52\,W\,cm^{-2}$ with a peak target power density of $1.1\,kW\,cm^{-2}$ for the voltage pulse duration of $200\,\mu s$. We note that this discharge regime was proved to be suitable for the deposition of densified, highly optically transparent, stoichiometric ZrO_2 films with a high deposition rate close to $120\,nm\,min^{-1}$.[5,6]

In the present paper, we use time-resolved optical emission spectroscopy (OES) to investigate the effects of the increased target power density (up to $3.0\,kW\,cm^{-2}$) applied in voltage pulses four times shorter (from 200 to $50\,\mu s$) at an almost equivalent deposition-averaged target power density of $53\,W\,cm^{-2}$ during the ZrO_2 film preparation.

II. EXPERIMENTAL DETAILS

A. Film preparation

Film deposition (see Refs. 5, 6, and 8 for more details) was carried out in a standard stainless-steel vacuum chamber (a diameter of 507 mm and a length of 520 mm) equipped with a strongly unbalanced magnetron source (a 99.9% Zr purity target with a diameter of 100 mm and a thickness of 6 mm). The magnetron was driven by a high-power pulsed dc power supply (HMP 2/1, Hüttinger Elektronik) at a repetition frequency of 500 Hz with voltage pulse durations t_{on} of 50 and $200\,\mu s$. The ZrO_2 films were deposited onto Si substrates located 100 mm from the target and held at a floating potential. The chamber was evacuated by a diffusion pump (a pump rate of $2\,m^3\,s^{-1}$) backed by a rotary pump (a pump rate of $30\,m^3\,h^{-1}$) down to a base pressure less than 1×10^{-3} Pa. During deposition, the argon partial pressure, p_{ar}, was kept constant at 2 Pa (a flow rate of 30 sccm). Oxygen was admitted directly into the plasma via two inlets (a diameter of 1 mm) located 25 mm from the target and

Note: This paper is part of the 2020 Special Topic Collection Festschrift Honoring Dr. Steve Rossnagel.

[a)]Electronic mail: vlcek@kfy.zcu.cz

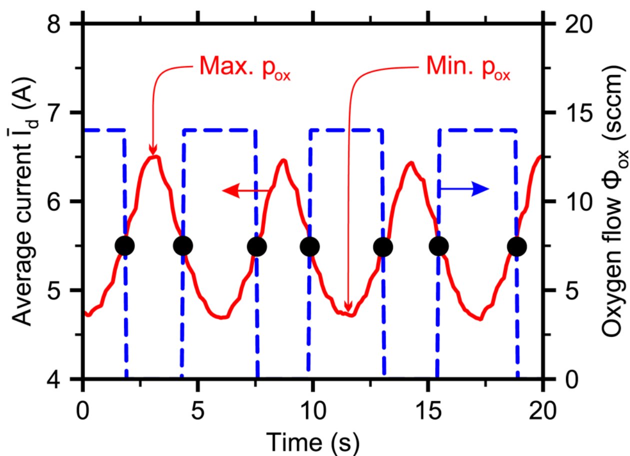

FIG. 1. Time evolution of the average discharge current in a period of the power supply, $\bar{I}_d$ (solid line), and the corresponding oxygen flow rate pulses, Φ_{ox} (dashed line), during a controlled reactive sputter deposition of the stoichiometric ZrO_2 film at $t_{on} = 50\,\mu s$ and $\langle S_d \rangle = 53\,\mathrm{W\,cm^{-2}}$. A preselected critical value of $\bar{I}_d = 5.5$ A (dots) determines the switching-on and switching-off of the oxygen flow rate $\Phi_{ox} = 14.0$ sccm.

oriented toward the substrate. The total pressure is given as $p_{ar} + p_{ox}$, where p_{ox} is the oxygen partial pressure, and was measured by a pressure sensor located at the chamber wall 270 mm from the target–substrate axis.

Using the magnetron voltage, $U_d(t)$, and the discharge current, $I_d(t)$, waveforms, the average target power density in a discharge pulse, S_{da}, and the deposition-averaged target power density, $\langle S_d \rangle$, were evaluated[5] using the following formulas:

$$S_{da} = \frac{1}{t_{on}} \int_0^{t_{on}} U_d(t) J_t(t)\, dt, \tag{1}$$

$$\langle S_d \rangle = \frac{1}{t_e - t_s} \int_{t_s}^{t_e} U_d(t) J_t(t)\, dt. \tag{2}$$

Here, the target current density $J_t(t) = I_d(t)/A_t$, where A_t is the total area of the target ($78.54\,\mathrm{cm^2}$), and t_s and t_e are the start and end times of the deposition, respectively. Note that S_{da} is time dependent during deposition as the discharge pulses are realized at time-varying p_{ox} on the scale of seconds (see Figs. 1 and 3). The time-varying average discharge current in a period, T, of the power supply, $\bar{I}_d$, was evaluated using the formula

$$\bar{I}_d = \frac{1}{T} \int_0^{T} I_d(t)\, dt. \tag{3}$$

The basic principle of the pulsed RGFC system is illustrated in Fig. 1 for the discharge regime with $t_{on} = 50\,\mu s$ and $\langle S_d \rangle = 53\,\mathrm{W\,cm^{-2}}$ (Table I). During the deposition, a programmable logic controller provides a control feedback signal to the two O_2 mass-flow controllers to adjust the pulsed O_2 flow rate into the conduits by adjusting the duration of the O_2 flow rate pulses by means of the preselected critical value of $\bar{I}_d(t)$. The critical value of $\bar{I}_d(t) = 5.5$ A determines the switching-on and switching-off of the oxygen flow rate $\Phi_{ox} = 14.0$ sccm (see Fig. 1). Under these conditions, the amount of oxygen injected into the high-density plasma in front of the sputtered target is sufficiently low to minimize the compound fraction in the target surface layer. However, this amount of oxygen is sufficiently high to achieve the required incorporation of the oxygen atoms into the films (stoichiometric ZrO_2 composition). The low compound fraction in the target surface layer is needed to minimize arcing on the target and increase the deposition rate of films. Recall that the preselected critical values of $\bar{I}_d(t) = 7.0$ A and $\Phi_{ox} = 16.8$ sccm were used for the discharge regime with $t_{on} = 200\,\mu s$ and $\langle S_d \rangle = 52\,\mathrm{W\,cm^{-2}}$.[6,8]

Table I shows the material characteristics of deposited films for both discharge regimes examined. In both cases, highly optically transparent stoichiometric ZrO_2 films were deposited. A more detailed information on the film characterization methods used, the obtained film properties, as well as the description of the deposition system and the principle of the pulsed RGFC system can be found in Refs. 5 and 6. In spite of the p_{ox} oscillations during film depositions, no multilayer structures of the films or periodic changes in their fully reproducible compositions and properties were observed. High-resolution transmission electron microscopy and electron diffraction proved vertically homogeneous microstructures of hard and optically transparent HfO_2 films prepared using this deposition technique.[9]

TABLE I. Deposition and material characteristics of the stoichiometric ZrO_2 films at the voltage pulse durations $t_{on} = 50$ and $200\,\mu s$. The oxygen partial pressure, p_{ox}, oscillated between 0 and 0.08 Pa. Here, $\langle S_d \rangle$ is the deposition-averaged target power density, S_{da} is the average target power density in a pulse, Φ_{ox} is the oxygen flow rate in an oxygen flow pulse, a_D is the deposition rate of the films, k_{550} and n_{550} are the extinction coefficient and refractive index of the films at a wavelength of 550 nm, respectively, and H is the hardness of the films.

	Deposition characteristics				Material characteristics		
t_{on} (μs)	$\langle S_d \rangle$ ($\mathrm{W\,cm^{-2}}$)	S_{da} ($\mathrm{W\,cm^{-2}}$)	Φ_{ox} (sccm)	a_D ($\mathrm{nm\,min^{-1}}$)	k_{550} (1×10^{-3})	n_{550}	H (GPa)
50	53.0	1700–2100	14.0	80	1.0	2.07	10
200	52.0	370–540	16.8	118	2.0	2.19	16

For a correct interpretation of the OES results, it is very important to take into account the substantially increased local oxygen partial pressure in front of the O_2 inlets. Our measurements,[10] which were similar to those performed by Rossnagel,[11] showed that the local values of the oxygen partial pressure at a position of 35 mm from the target surface (i.e., 10 mm from the O_2 inlets) oscillated between a minimum of 0.03 Pa and a maximum of 0.24 Pa, while the value of p_{ox} measured at the wall of the vacuum chamber oscillated between 0 and 0.08 Pa under the discharge conditions investigated (Table I).

B. Optical emission spectroscopy and derived quantities

The OES system with time resolution (see Ref. 8 for more details) consisted of a grating spectrometer (Jobin-Yvon THR 1000, 1800 gr mm^{-1}), a photomultiplier tube (Hamamatsu R 3896), and a photon counter (Stanford Research Systems SR 430). The light was collected by a rectangular (10×15 mm) collimator (length of 450 mm), positioned perpendicular to the discharge axis.[8] The light was collected at two distances from the target; namely, at $z = 10$ mm (near the target) and at $z = 50$ mm (in the plasma bulk). The OES system was synchronized with the initiations of the voltage pulses by a high-speed comparator with an additional logic, allowing us to trigger the measurements close to maximum and minimum p_{ox} during depositions (Fig. 3). Photon counts relating to the corresponding emission lines were recorded with a time resolution of 320 ns for several thousand voltage pulses to achieve a high signal-to-noise ratio.

We use the methodology presented in Ref. 8 for signal processing of the same optical emission lines therein: Ar 750.39 nm with the excitation energy of the upper level of $E_m = 13.48$ eV, Ar^+ 487.99 nm with $E_m = 19.68$ eV, O 844.64 nm with $E_m = 10.99$ eV, O^+ 374.95 nm with $E_m = 26.30$ eV, Zr 515.55 nm with $E_m = 3.99$ eV, Zr^+ 292.70 nm with $E_m = 5.99$ eV, Zr^+ 346.30 nm with $E_m = 5.07$ eV, Zr^+ 414.92 nm with $E_m = 3.79$ eV, and Zr^{2+} 288.67 nm with $E_m = 7.40$ eV. It resulted in the determination of the excited-state population $n_m(X)$ for a selected particle X using $n_m(X) = N_m(X)/A_{mk}$, where $N_m(X)$ is the photon count per second relating to the corresponding emission line and A_{mk} is the respective transition probability given in Ref. 8. Here, it should be mentioned that the Zr^+ 346.30 nm and 414.92 nm lines were used only for the determination of the excitation temperatures.

We assume that the dominant population process for the upper levels of the selected optical emission lines is the electron-impact (direct and stepwise) excitation from the corresponding ground states and their dominant depopulation process is spontaneous radiation under the HiPIMS conditions investigated. Thus, the relation for the excited-state population $n_m(X)$ can be written as

$$n_m(X) \propto n_1(X) n_e C_m^X(T_e), \tag{4}$$

where $n_1(X)$ is the ground-state population; n_e and T_e are the electron density and temperature, respectively; and $C_m^X(T_e)$ is a rate coefficient, generally given by a collisional-radiative model for the considered particles in a discharge plasma.

Using the scaling $J_t \propto n_e T_e^{1/2}$, where n_e and T_e are the corresponding values at the plasma-sheath interface, relation (4) can be rewritten in a form valid for $n_1(X)$ near the target sheath, such that

$$n_1(X) \propto \frac{n_m(X)}{J_t} \frac{T_e^{1/2}}{C_m^X(T_e)}. \tag{5}$$

For T_e constant in time near the target during the voltage pulses, the $n_m(X)/J_t$ ratios characterize trends in the time evolution of the local ground-state populations $n_1(X)$.

Using relation (4), we obtain relation (6) for the $n_1(X)/n_1(Y)$ ratio, valid not only near the target sheath but also in the plasma bulk,

$$\frac{n_1(X)}{n_1(Y)} \propto \frac{n_m(X)}{n_{m'}(Y)} \frac{C_{m'}^Y(T_e)}{C_m^X(T_e)}, \tag{6}$$

where X and Y are the chosen particles. For T_e constant in time during the voltage pulses, the $n_m(X)/n_{m'}(Y)$ ratios characterize trends in the time evolution of the local ground-state density ratios $n_1(X)/n_1(Y)$.

It was shown in the literature[12–15] that the excitation temperature, T_{ex}, determined from the slope of the Boltzmann plots[16,17] follows trends of T_e, particularly in discharges with sufficiently high n_e values. However, the values of T_{ex} and T_e can be different. The Boltzmann plots measured for $z = 10$ mm (see Fig. 2) and $z = 50$ mm exhibited a rapid establishment of equilibrium between electrons in a high-density plasma and the excited states of Zr^+ ions during voltage pulses. Therefore, we used these plots to determine the T_{ex} values. It is important that the chosen Zr^+ lines do not overlap with other lines in the spectrum and that their transition probabilities, A_{mk}, are relatively high. Moreover, the excitation energies of the corresponding upper levels are sufficiently different from each other with $E_m \leq 5.99$ eV. These E_m values are low enough to avoid the effect of a charge transfer between the Ar^+ ions and Zr atoms in ground states, which produce excited Zr^+ ions with the excitation energies $E_m \geq 9.13$ eV.[8]

III. RESULTS AND DISCUSSION

A. Discharge characteristics

The time evolution of the magnetron voltage, $U_d(t)$, and the target current density, $J_t(t)$, for $t_{on} = 50\,\mu s$ and $\langle S_d \rangle = 53$ W cm^{-2}, and for $t_{on} = 200\,\mu s$ and $\langle S_d \rangle = 52$ W cm^{-2} are depicted in Fig. 3. Because the value of p_{ox} alternates on the scale of seconds as the RGFC system opens and closes the O_2 flow into the conduits, the $U_d(t)$ and $J_t(t)$ waveforms oscillate between their maximum (Max. p_{ox}) and minimum (Min. p_{ox}) curves. The ranges of the $J_t(t)$ waveforms during the OES measurements close to the maximum p_{ox} (the shaded areas between the dotted and solid lines) and minimum p_{ox} (the shaded areas between the dotted and dashed lines) are shown in Fig. 3.

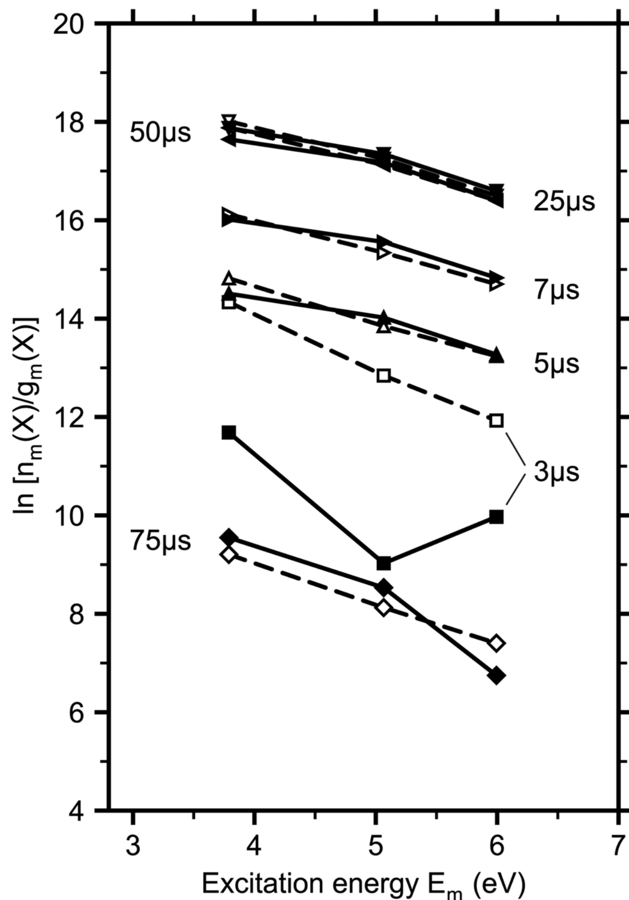

FIG. 2. Boltzmann plots constructed from the populations $n_m(X)$ of three different excited states [with the statistical weights $g_m(X)$ given in Ref. 8] of the Zr^+ ion measured during a pulse with $t_{on} = 50\,\mu s$, and $25\mu s$ after its termination for $z = 10$ mm. The values measured close to the maximum (solid lines) and minimum (dashed lines) p_{ox} during a film deposition (Fig. 3) are shown.

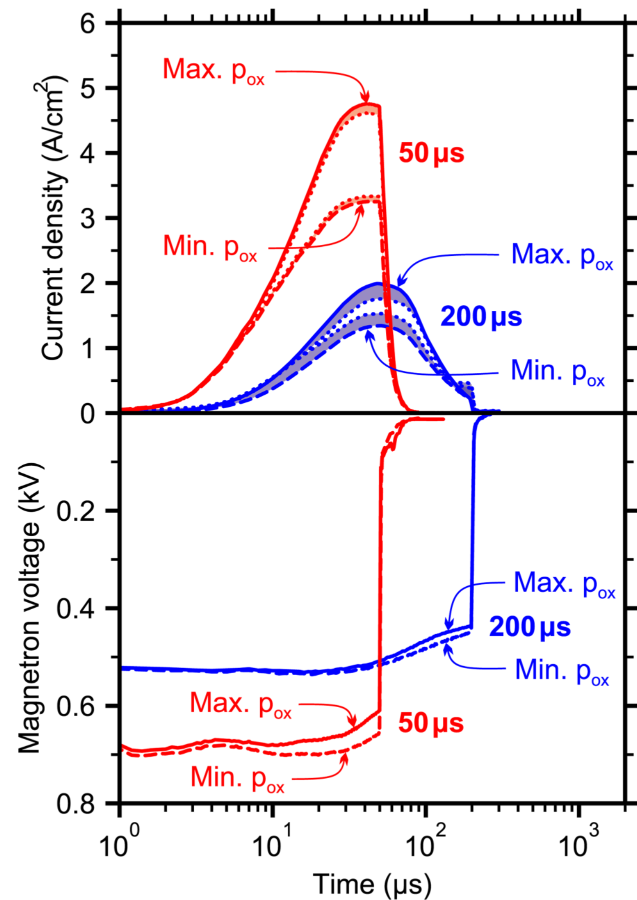

FIG. 3. Magnetron voltage, U_d, and the target current density, J_t, during pulses with $t_{on} = 50$ and $200\,\mu s$. The dotted lines represent the start and termination of the OES measurements close to the maximum (solid lines) and minimum (dashed lines) p_{ox} during film depositions.

Recall that the higher values of $J_t(t)$ at the higher p_{ox} can be caused by three factors:[8] (i) a higher secondary-electron emission coefficient of a Zr target partially covered by an oxide,[18] (ii) a supplemental bombardment of the target by oxygen ions (atomic or molecular), and (iii) a possibly higher secondary-electron emission coefficient induced by O^+ and O_2^+ ions than that induced by Ar^+ ions.[19,20]

Owing to the oscillations of the $U_d(t)$ and $J_t(t)$ waveforms, the S_{da} values and the peak target power density in a pulse, S_{peak}, can exhibit a range of values. In particular, S_{da} ranges from 1.7 to 2.1 kW cm^{-2} and S_{peak} ranges from 2.2 to 3.0 kW cm^{-2} for $t_{on} = 50\,\mu s$ and $\langle S_d \rangle = 53$ W cm^{-2}. For $t_{on} = 200\,\mu s$ and $\langle S_d \rangle = 52$ W cm^{-2}, S_{da} ranges from 0.4 to 0.5 kW cm^{-2}, and S_{peak} ranges from 0.9 to 1.1 kW cm^{-2}.

Both discharge regimes exhibit a rapid onset of J_t (note the logarithmic time scale in Fig. 3). This indicates a very low compound fraction in the target surface layer at the beginning of the voltage pulses in comparison with HiPIMS discharges operating in an oxide mode.[20–22] As expected, the higher absolute value of U_d (by approximately 170 V) leads to a much more rapid onset of J_t in the case of the shorter high-power pulses.

References 10 and 23 present the results obtained from a parametric model, which takes into account the specific features of HiPIMS discharges together with a possible increase in the density of reactive gas in front of the reactive gas inlets immersed into the plasma. The calculations showed that the compound (ZrO_2) fractions in the target surface layer, Θ_{ts}, are very low for both discharge regimes examined here. The values of Θ_{ts} were lower than 12% and 8% for $t_{on} = 50$ and $200\,\mu s$, respectively, at the same $\langle S_d \rangle = 50$ W cm^{-2} and $p_{ox} = 0.05$ Pa, where the latter value is close to the mean value of p_{ox} during the controlled oscillations in experiments. The higher values of Θ_{ts} for $t_{on} = 50\,\mu s$ are caused mostly by a higher chemisorption flux of oxygen particles onto the target during the pulse-off time. This higher flux is owing to a substantially increased dissociation of O_2 molecules in the discharge with a four times higher $S_{da} = 2.0$ kW cm^{-2} than for $t_{on} = 200\,\mu s$ with $S_{da} = 0.5$ kW cm^{-2}.[10]

B. Time evolution of the excitation temperatures

Figure 4 shows the time evolution of the excitation temperature, T_{ex}, determined from the slope of the Boltzmann plots for the excited-state populations of Zr^+ ions at the position $z = 10$ and 50 mm for both discharge regimes. Only the

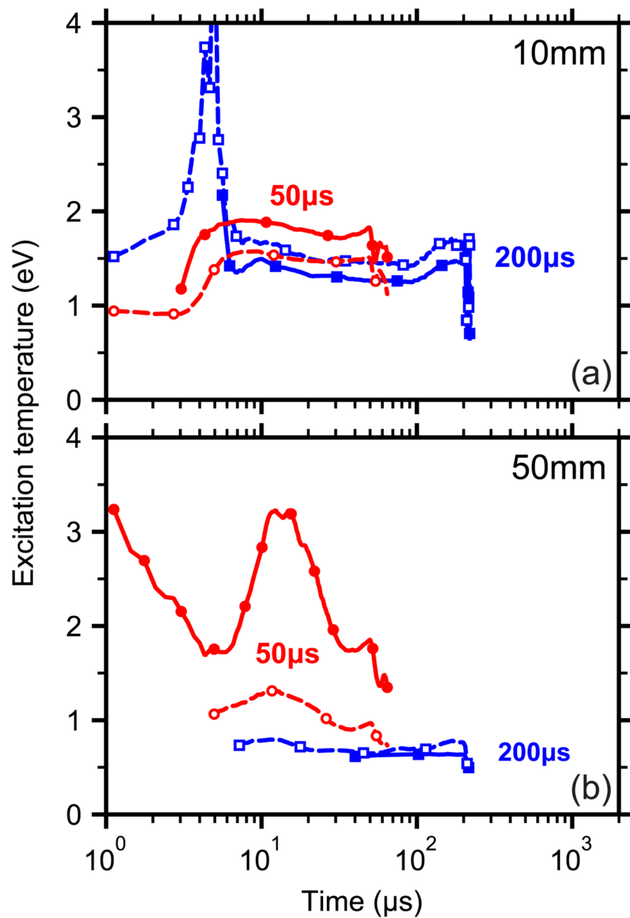

FIG. 4. Excitation temperature, T_{ex}, during pulses with $t_{on} = 50\,\mu s$ (circles) and $200\,\mu s$ (squares) for $z = 10$ mm (a) and $z = 50$ mm (b). The values measured close to the maximum (solid lines) and minimum (dashed lines) p_{ox} during film depositions (Fig. 3) are shown.

T_{ex} values with a relative measurement error less than 25% are presented. Near the target ($z = 10$ mm), the relative error was less than 2.5% for T_{ex} measured between $t = 5$ and $50\,\mu s$ for $t_{on} = 50\,\mu s$ and $\langle S_d \rangle = 53\,W\,cm^{-2}$, when T_{ex} was approximately constant between $t = 7$ and $50\,\mu s$. For $t_{on} = 200\,\mu s$ and $\langle S_d \rangle = 52\,W\,cm^{-2}$, the relative error was less than 10% for T_{ex} at the beginning of the voltage pulses and less than 5% for T_{ex} measured, when it was approximately constant, between $t = 7$ and $200\,\mu s$.

The initial increase in T_{ex} near the target between $t = 3$ and $5\,\mu s$ for $t_{on} = 200\,\mu s$ is caused by an avalanche of high-energy electrons.[24,25] These high-energy electrons are delayed by the time of transport across the magnetic field above the target to the distance of measurement ($z = 10$ mm) and are simultaneously cooled down by inelastic collisions with mainly Ar and Zr atoms that remain in front of the target from the previous voltage pulse. In contrast to the regime with $t_{on} = 200\,\mu s$, no T_{ex} peak is observed at $z = 10$ mm for the high-power regime with $t_{on} = 50\,\mu s$. The reason is a rapid rise in the number of Zr atoms sputtered from the target owing to the rapid onset of J_t during a pulse (see Fig. 3), and their frequent excitations and ionizations leading to a consumption of electron energy. From $t = 7\,\mu s$ up to the voltage pulse termination, the values of T_{ex} remain almost constant (1.5–1.6 eV and 1.7–1.9 eV for the measurements close to the minimum and maximum p_{ox}, respectively) during voltage pulses at $t_{on} = 50\,\mu s$ and $\langle S_d \rangle = 53\,W\,cm^{-2}$. These values are similar to the corresponding $T_{ex} = 1.5–1.7$ eV (close to p_{ox} minimum) and $T_{ex} = 1.3–1.5$ eV (close to p_{ox} maximum) measured at $z = 10$ mm from $t = 7\,\mu s$ for $t_{on} = 200\,\mu s$.

In the bulk plasma ($z = 50$ mm), T_{ex} is approximately constant in large parts of the voltage pulses, with values between 0.7 and 0.8 eV for $t_{on} = 200\,\mu s$ and values between 0.9 and 1.3 eV close to the minimum p_{ox} for $t_{on} = 50\,\mu s$. There is an exception, however, for $t_{on} = 50\,\mu s$ close to the maximum p_{ox}. In this case, when the S_{peak} rapidly increases up to $3.0\,kW\,cm^{-2}$ (Fig. 3), the value of T_{ex} steeply rises again after an initial cooling. A double peak is formed around $t = 12\,\mu s$ with $T_{ex} = 3.2$ eV, and then a gradual decrease occurs toward the termination of the voltage pulse. The peak of T_{ex} signifies that hotter electrons may penetrate from the target region into the plasma bulk. This is not only true during the first electron avalanche at the initiation of the voltage pulse, but some mechanism of their escape from the magnetic trap must also exist during the voltage pulse. It is well known that localized light patterns, also known as plasma spokes or ionization zones, are present in nonreactive and reactive HiPIMS discharges.[26,27] The plasma spokes are responsible not only for the generation of ions with enhanced energies[28,29] in the flux onto a substrate but also for additional heating of the electrons in front of the target[30,31] and for the escape of electrons from the target region.[30] The decrease in T_{ex} after $t = 16\,\mu s$ for $t_{on} = 50\,\mu s$ close to the maximum p_{ox} is caused by cooling of electrons in their ionization and excitation collisions as a result of the increasing content of Zr atoms and ions in the plasma bulk.

As is seen in Fig. 4, the increase in p_{ox} leads to a rise in T_{ex} at both measurement positions for the high-power discharge regime with $t_{on} = 50\,\mu s$. This behavior is opposite to that of the regime with $t_{on} = 200\,\mu s$, where a higher content of oxygen in the discharge induces a reduction in T_{ex}. Note that the literature has reported both an increase[32,33] and decrease[34,35] in the electron temperature with an increase in the content of oxygen in various magnetron discharges.

C. Trends of the ground-state densities

Considering the results obtained for T_{ex} (Fig. 4), we now take the electron temperature, T_e, appearing in relation (5), to be constant near the target ($z = 10$ mm) from $t = 7\,\mu s$ for both discharge regimes. Then, the respective $n_m(X)/J_{th}$ and $n_m(X)/J_{tl}$ ratios in Fig. 5 characterize trends in time evolution of the local ground-state densities, $n_1(X)$, for the considered particles [relation (5)] near the target during the voltage pulses close to the maximum and minimum p_{ox}. Here, it should be noted that the values of $J_{th}(t)$ and $J_{tl}(t)$ are the average target current densities at the time t of the voltage pulses during the OES measurements[8] close to the maximum and minimum p_{ox}, respectively (see the shaded areas in Fig. 3).

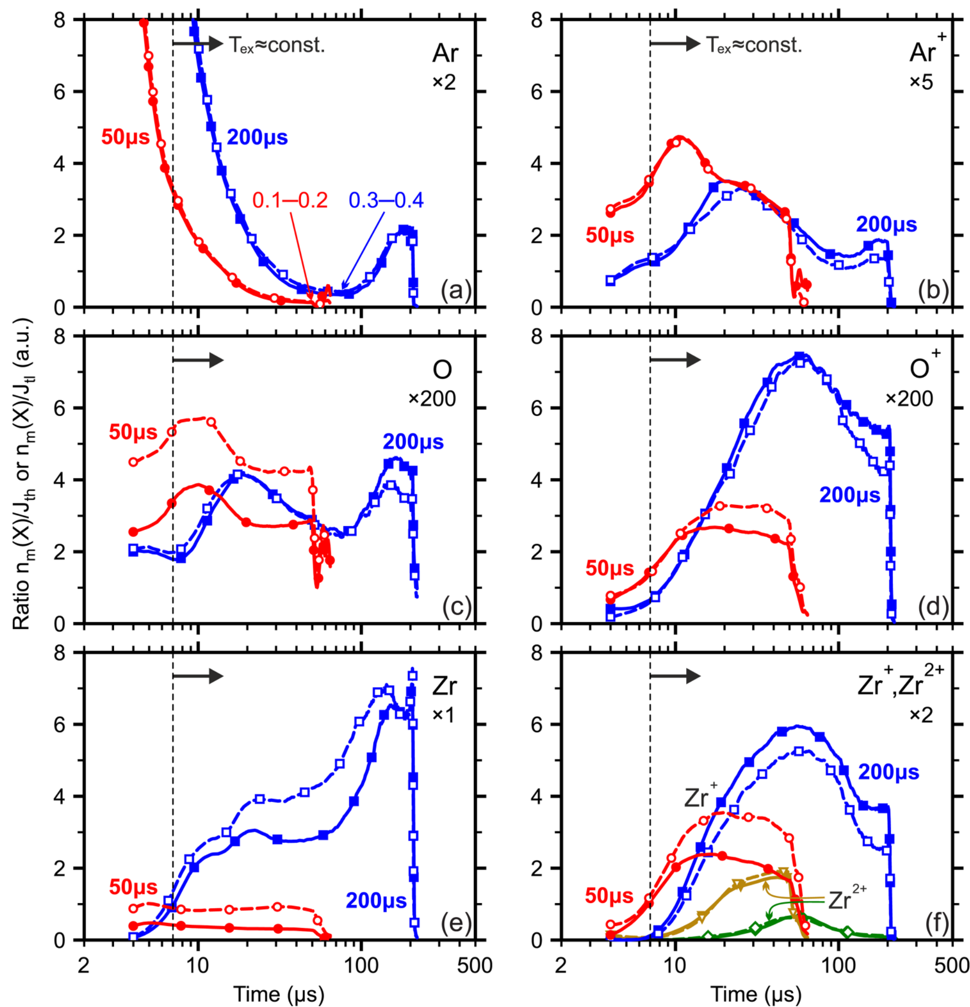

FIG. 5. $n_m(X)/J_{th}$ and $n_m(X)/J_{tl}$ ratios for $X = \mathrm{Ar}$ (a), Ar^+ (b), $X = \mathrm{O}$ (c), O^+ (d), $X = \mathrm{Zr}$ (e), Zr^+ and Zr^{2+} (f) during pulses with $t_{on} = 50\,\mu s$ (circles and triangles) and $200\,\mu s$ (squares and diamonds) for $z = 10$ mm. The $n_m(X)/J_{th}$ values measured close to the maximum p_{ox} during deposition (solid lines) (Fig. 3) and the $n_m(X)/J_{tl}$ values measured close to the minimum p_{ox} during the deposition (dashed lines) are shown. The broken vertical line represents the first time from which T_{ex} remains almost constant (Fig. 4) up to the termination of the voltage pulses for $z = 10$ mm. Here, $n_m(X)$ is the excited-state population, J_{th} and J_{tl} are the average target current densities during the OES measurements close to the maximum and minimum p_{ox}, respectively.

As expected, a substantial increase in the power, delivered into the discharge for $t_{on} = 50\,\mu s$, results in a more rapid and greater reduction of the Ar atom density near the target. We recall here that the Ar atom density reduction has several mechanisms: (i) The first is a rarefaction of the Ar atom density owing to a momentum transfer from the sputtered Zr atoms.[2,36,37] (ii) The second is heating of Ar atoms[11,38] in collisions with sputtered particles. (iii) The third is an electron-impact ionization producing Ar^+ ions.[38,39] Taking into account the small difference between T_{ex} (less than 0.4 eV) for both discharge regimes (Fig. 4), the measured ratios $n_m(\mathrm{Ar})/J_{th}$ and $n_m(\mathrm{Ar})/J_{tl}$ (Fig. 5) may be used for a rough comparison of time-dependent ground-state densities $n_1(\mathrm{Ar})$ during the pulses with $t_{on} = 50$ and $200\,\mu s$. Thus, it may be stated that the minimum Ar density for the high-power regime with $t_{on} = 50\,\mu s$ is roughly one half of that for the regime with $t_{on} = 200\,\mu s$. This is in agreement with the model assumptions in Refs. 10 and 23.

The density of Ar^+ ions increases at the voltage pulse initiation for both regimes examined. This is a consequence of the increasing probability of the already-mentioned electron-impact ionization of Ar atoms as the density of electrons increases near the target. For $t_{on} = 50\,\mu s$, the Ar^+ ion density reaches its maximum around $t = 11\,\mu s$, whereupon it gradually reduces up to the termination of the voltage pulse. The reduction of Ar^+ ion density is caused by (i) the reduction of the Ar atom density; (ii) a backward flux of the Ar^+ ions onto the target; (iii) fluxes of the Ar^+ ions toward the substrate and chamber walls; (iv) the electron-impact ionization of Ar^+ ions producing Ar^{2+} ions (Ar^{2+} ions were not monitored in this work); and (iv) a possible charge transfer, mainly with sputtered Zr atoms, producing Zr^+ ions.[40]

For the analysis of the time evolutions of the O atom and O^+ ion ground-state density, one needs to take into account that O atoms are produced predominantly by an effective dissociation process with a relatively low threshold energy of 5.12 eV (Ref. 41) from O_2 molecules introduced by the inlets immersed in the plasma and placed 25 mm from the target. Further, one must consider that the O atoms produced by this dissociation process may have additional kinetic

energy (see repulsing states of O_2 molecules[41]) promoting their diffusion in the discharge volume. In spite of the low compound fractions in the target surface layer [$\Theta_{ts} < 20\%$ for the maximum $p_{ox} = 0.08$ Pa (Ref. 10)] and the high degree of dissociation of the O_2 molecules in our case, the O atoms sputtered from the target also contribute to their occurrence in the discharge plasma.[42] In general, the time evolutions of the ground-state densities of O atoms and O^+ ions exhibit similarities (rarefaction effect, electron-impact ionization of atoms and ions, fluxes of ions toward the substrate and chamber walls, and backward flux of ions onto the target) with the time evolutions of the ground-state densities of Ar atoms and Ar^+ ions, respectively, for both regimes examined. A considerably lower $n_m(\mathrm{O})/J_{th}$ measured close to the maximum p_{ox} in comparison with the $n_m(\mathrm{O})/J_{tl}$ measured close to the minimum p_{ox} for $t_{on} = 50\,\mu$s was found. This difference may be explained mainly by the substantially higher probability of the electron-impact ionization of O atoms in the high-density plasma in front of the target, as well as by the lower diffusion of O_2 molecules and O atoms against the much stronger sputtering wind at the elevated target current density (see Fig. 3) for the maximum p_{ox}. Note also the higher value of T_{ex} at the maximum p_{ox} for $t_{on} = 50\,\mu$s. This value promotes the electron-impact processes forming the O_2^+ (a threshold energy of 12.06 eV) and O^+ ions (a threshold energy of 19.5 eV) directly from O_2 molecules,[43–45] leading to a lower density of O atoms.

We next consider the mechanism behind the decreased $n_1(\mathrm{O}^+)$ density characterized at the position $z = 10$ mm from the target during the high-power pulses with $t_{on} = 50\,\mu$s (Fig. 5). The reason for this decreased density may be the higher flux of O^+ ions formed close to the target ($z < 10$ mm) at the much higher $S_{da} = 1.7$–$2.1\ \mathrm{kW\,cm^{-2}}$ than that formed during the longer pulses with $t_{on} = 200\,\mu$s and $S_{da} = 0.4$–$0.5\ \mathrm{kW\,cm^{-2}}$ onto the target.

Unlike the discharge regime with $t_{on} = 200\,\mu$s, where the ground-state density of sputtered Zr atoms, $n_1(\mathrm{Zr})$, increases during a voltage pulse; $n_1(\mathrm{Zr})$ remains low and almost constant in time during a voltage pulse with $t_{on} = 50\,\mu$s. This is a result of intense electron-impact ionization of Zr atoms (an ionization energy of 6.63 eV) and Zr^+ ions (an ionization energy of 13.16 eV[40]) close to the target at very high S_{da} values. Here, we note that the measured $n_m(X)/J_t$ ratios (Fig. 5) cannot be used for a direct comparison of the ground-state densities $n_1(\mathrm{Zr})$, $n_1(\mathrm{Zr}^+)$, and $n_1(\mathrm{Zr}^{2+})$ during the voltage pulses with the same t_{on}. This is mainly owing to a decreasing rate coefficient $C_m^X(T_e)$ in relation (5) with an increase in excitation energy E_m, which are 3.99, 5.99, and 7.40 eV for the mth state of the Zr atoms, Zr^+ ions, and Zr^{2+} ions, respectively. As a result, the measured $n_m(X)/J_t$ ratios lead to underestimated relative values of $n_1(\mathrm{Zr}^+)$, and particularly $n_1(\mathrm{Zr}^{2+})$, in comparison with $n_1(\mathrm{Zr})$ under the same discharge conditions. Note that the $n_1(\mathrm{Zr}^+)$ and $n_1(\mathrm{Zr}^{2+})$ densities characterized at the position $z = 10$ mm from the target during the high-power pulses with $t_{on} = 50\,\mu$s (Fig. 5) can be more reduced by a higher backward flux of the Zr^+ and Zr^{2+} ions onto the target[10] than during the longer pulses with $t_{on} = 200\,\mu$s. We note that most of the Zr^+ and Zr^{2+} ions are formed close to the target ($z < 10$ mm).

D. Trends of the ground-state density ratios

Figures 6–8 show the time evolutions of the $n_m(X)/n_{m'}(Y)$ population ratios for various X and Y particle pairs measured during both discharge regimes near the target ($z = 10$ mm) and in the plasma bulk ($z = 50$ mm). With respect to the results obtained for T_{ex} (Fig. 4), we consider the electron temperature, T_e [appearing in relation (6)], constant not only near the target but also in the plasma bulk in the large parts of the voltage pulses. The only exception is a nonconstant T_e in the plasma bulk during the high-power pulses with $t_{on} = 50\,\mu$s close to the maximum p_{ox}. At the constant T_e, the respective $n_m(X)/n_{m'}(Y)$ ratios in Figs. 6–8 characterize trends in the time evolution of the local ground-state density ratios, $n_1(X)/n_1(Y)$, for the chosen particles [relation (6)] near the target and in the plasma bulk during the voltage pulses. There exists only a small difference between the T_{ex} for both discharge regimes at $z = 10$ mm and for both discharge regimes close to the minimum p_{ox} at $z = 50$ mm. Therefore, the measured ratios $n_m(X)/n_{m'}(Y)$ may be used for a rough comparison of the corresponding time-dependent ratios $n_1(X)/n_1(Y)$ during the voltage pulses with $t_{on} = 50$ and $200\,\mu$s at the same position in the vacuum chamber. Here, it should be mentioned that the different values of T_{ex}

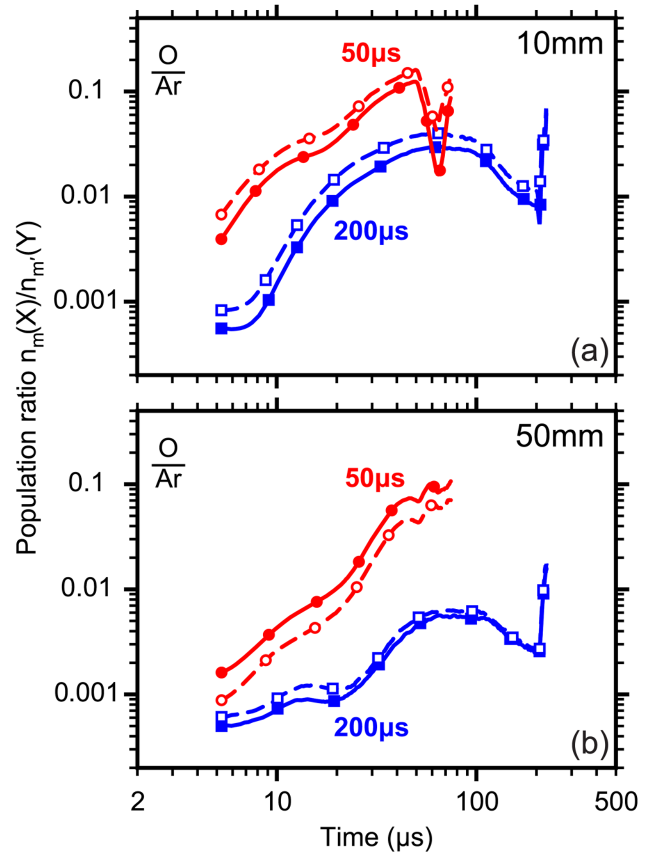

FIG. 6. Similar to Fig. 4, but for the $n_m(\mathrm{O})/n_{m'}(\mathrm{Ar})$ population ratio at $z = 10$ mm (a) and $z = 50$ mm (b).

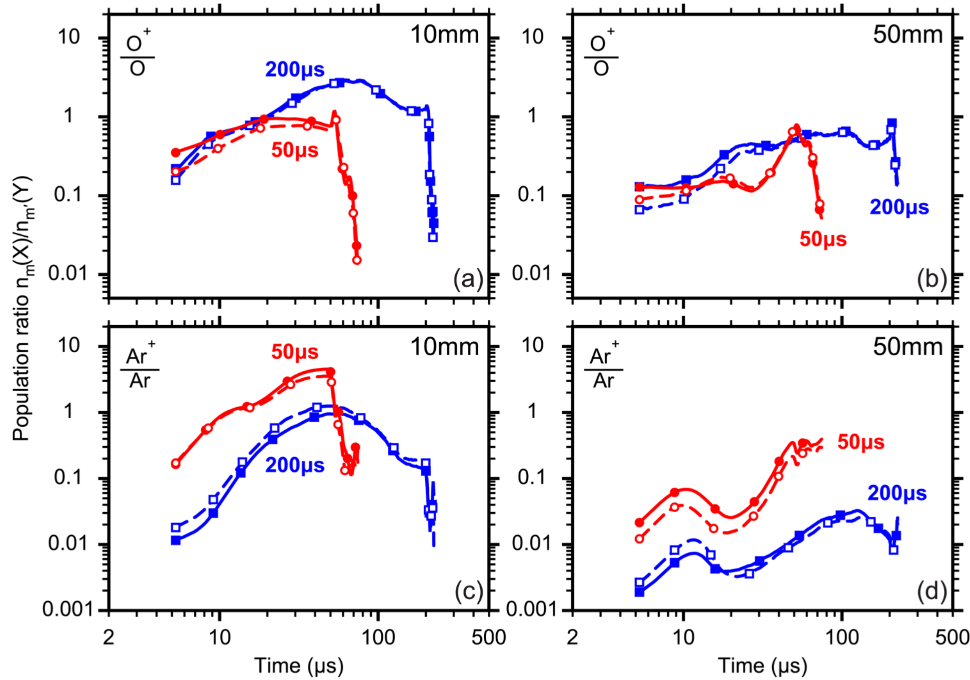

FIG. 7. Similar to Fig. 4, but for the $n_m(O^+)/n_{m'}(O)$ population ratio (a) and (b) and the $n_m(Ar^+)/n_{m'}(Ar)$ population ratio (c) and (d).

and their different time evolutions measured at the position $z = 50$ mm from the target during the pulses with $t_{on} = 50\,\mu s$ close to the maximum and minimum p_{ox} (Fig. 4) did not result in greater differences between the corresponding $n_m(X)/n_{m'}(Y)$ ratios than in the case of the pulses with $t_{on} = 200\,\mu s$ (see Figs. 6–8).

The trends in the $n_1(O)/n_1(Ar)$ ratio and in the degree of ionization of the O and Ar atoms at both positions during the discharge pulses are characterized in Figs. 6 and 7, respectively. As is seen in Fig. 6, the $n_m(O)/n_{m'}(Ar)$ ratio rapidly increases for $z = 10$ mm, particularly during high-power pulses with $t_{on} = 50\,\mu s$. This is mainly owing to the greater reduction of the Ar atom density than the O atom density (see Fig. 5), where the former is caused by the strong rarefaction and heating of the Ar gas and by the intense electron-impact ionization of Ar atoms (see Fig. 7).

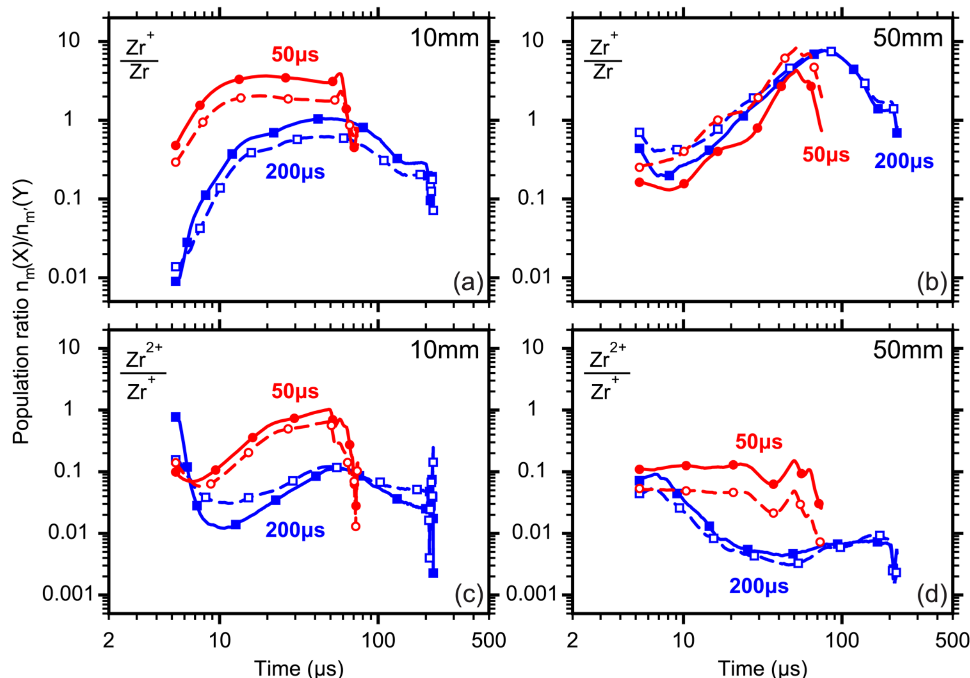

FIG. 8. Similar to Fig. 4, but for the $n_m(Zr^+)/n_{m'}(Zr)$ population ratio (a) and (b) and the $n_m(Zr^{2+})/n_{m'}(Zr^+)$ population ratio (c) and (d).

The main reason for the slower decrease of the O atom density near the target during these pulses (see Fig. 5) is an increasing dissociation of the O_2 molecules diffusing from the O_2 inlets to the target. Note that the amount of the O_2 gas injected into the discharge is different during the two deposition regimes, leading to different deposition rates for the stoichiometric ZrO_2 film preparation (Table I). As is seen in Fig. 6, the $n_m(\mathrm{O})/n_{m'}(\mathrm{Ar})$ ratio also rapidly increases at the position $z = 50$ mm from the target, particularly during the voltage pulses with $t_{on} = 50\,\mu$s. Consider the weak rarefaction and heating of the Ar gas and significantly weaker electron-impact ionization of the Ar atoms (see Fig. 7) at this position compared with $z = 10$ mm. Thus, the high $n_m(\mathrm{O})/n_{m'}(\mathrm{Ar})$ ratio during the pulses with $t_{on} = 50\,\mu$s is caused mainly by an effective dissociation of the O_2 molecules injected from the inlets located 25 mm from the target and oriented toward the substrate (see the aforementioned substantial increase in the local oxygen partial pressure in front of the inlets). This is in agreement with the energy-resolved mass spectroscopy results obtained under the same discharge conditions. These latter results show, for $t_{on} = 50\,\mu$s and $\langle S_{da}\rangle = 53$ W cm^{-2}, the dominance of O^+ ions over O_2^+ ions in the total ion flux at the substrate position located 100 mm from the target.[6]

The trends in the degree of ionization of Zr atoms (from which Zr^+ ions are formed) and that of Zr^+ ions (from which Zr^{2+} ions are formed) at both positions in the vacuum chamber during the discharge pulses are characterized in Fig. 8. From the time evolution of the $n_m(\mathrm{Zr}^+)/n_{m'}(\mathrm{Zr})$ ratio in Fig. 8, it is clearly seen that a high number of sputtered Zr atoms are almost immediately ionized near the target at the initial moment of the high-power pulses with $t_{on} = 50\,\mu$s, regardless of the value of p_{ox}. The $n_m(\mathrm{Zr}^{2+})/n_{m'}(\mathrm{Zr}^+)$ ratio follows the same trend near the target but with only a short delay under these conditions. After roughly 11 μs, the $n_m(\mathrm{Zr}^+)/n_{m'}(\mathrm{Zr})$ ratio saturates, but the $n_m(\mathrm{Zr}^{2+})/n_{m'}(\mathrm{Zr}^+)$ ratio increases up to the termination of the high-power pulses. This behavior is different from the time evolutions of both ratios during the pulses with $t_{on} = 200\,\mu$s, when these ratios start to fall after 60 μs in accordance with the time evolution of the power delivered into the discharge plasma (see Fig. 3). The substantially higher values of both of the ratios measured at the position $z = 10$ mm during the high-power discharge regime with $t_{on} = 50\,\mu$s indicate much higher ionization degrees of Zr atoms and Zr^+ ions near the target than those achieved during the discharge regime with $t_{on} = 200\,\mu$s.

We note the similar values of the $n_m(\mathrm{Zr}^+)/n_{m'}(\mathrm{Zr})$ ratio in the plasma bulk ($z = 50$ mm) during both discharge regimes. The reason for these similar values is a higher flux of the Zr^+ ions, formed during the high-power pulses with $t_{on} = 50\,\mu$s in front of the target ($z < 50$ mm), traveling back onto the target than in the case of the pulses with $t_{on} = 200\,\mu$s. The higher backward flux of the Zr^+ and Zr^{2+} ions onto the target during the high-power regime with $t_{on} = 50\,\mu$s is one of the main reasons for a significant (by 34%) decrease of the $a_D/\langle S_d\rangle$ ratio.[10,23] This ratio characterizes the efficiency of the magnetron sputtering and the transfer of sputtered particles to the substrate.[46] Specifically, the $a_D/\langle S_d\rangle$ value decreased from 3.8 μm^3 kJ^{-1} for $t_{on} = 200\,\mu$s to 2.5 μm^3 kJ^{-1} for $t_{on} = 50\,\mu$s (see Table I). As is seen in Fig. 8, the $n_m(\mathrm{Zr}^{2+})/n_{m'}(\mathrm{Zr}^+)$ ratio is much higher during the pulses with $t_{on} = 50\,\mu$s than with $t_{on} = 200\,\mu$s, not only for $z = 10$ mm but also for $z = 50$ mm from the target. This is in agreement with the energy-resolved mass spectroscopy results obtained under the same discharge conditions showing, for $t_{on} = 50\,\mu$s and $\langle S_d\rangle = 53$ W cm^{-2}, a higher fraction of Zr^{2+} ions compared with Zr^+ ions in the total ion flux at the substrate position located 100 mm from the target.[6]

IV. CONCLUSIONS

Time-resolved optical emission spectroscopy was carried out near the sputtered Zr target ($z = 10$ mm) and in the plasma bulk ($z = 50$ mm). The measurements were obtained during reactive HiPIMS deposition of ZrO_2 films with a pulsed oxygen flow control and to-substrate O_2 inlets injecting oxygen gas into a high-density plasma in front of the target.

The main aim of this paper was to investigate the effects of the increased target power density (up to 3.0 kW cm^{-2}) applied in voltage pulses four times shorter (from 200 to 50 μs) at almost the same deposition-averaged target power density $\langle S_d\rangle \cong 50$ W cm^{-2} and a fixed repetition frequency of 500 Hz.

It was shown that the sputtered Zr atoms are much more ionized (with a high fraction of Zr^{2+} ions) and the Ar atom density is more decreased near the target during the high-power pulses with $t_{on} = 50\,\mu$s at a four times higher pulse-averaged target power density $S_{da} = 1.7$–2.1 kW cm^{-2} during the deposition. Under these conditions, the minimum Ar density near the target can be estimated as one half of that for the discharge regime with $t_{on} = 200\,\mu$s.

The much higher densities of O atoms and Zr^{2+} ions measured in the plasma bulk during the high-power discharge regime with $t_{on} = 50\,\mu$s are in agreement with the results obtained under the same conditions using an energy-resolved mass spectroscopy.[6]

The higher backward flux of the Zr^+ and Zr^{2+} ions onto the target during the high-power regime is one of the main reasons for a significantly (by 34%) decreased the efficiency of the magnetron sputtering and the transfer of sputtered particles to the substrate.

ACKNOWLEDGMENTS

This work was supported by the Czech Science Foundation under Project No. 17-08944S.

[1] K. Sarakinos, J. Alami, and S. Konstantinidis, Surf. Coat. Technol. **204**, 1661 (2010).

[2] J. T. Gudmundsson, N. Brenning, D. Lundin, and U. Helmersson, J. Vac. Sci. Technol. A **30**, 030801 (2012).

[3] D. Lundin and K. Sarakinos, J. Mater. Res. **27**, 780 (2012).

[4] A. Anders, J. Appl. Phys. **121**, 171101 (2017).

[5] J. Vlček, J. Rezek, J. Houška, R. Čerstvý, and R. Bugyi, Surf. Coat. Technol. **236**, 550 (2013).

[6]J. Vlček, J. Rezek, J. Houška, T. Kozák, and J. Kohout, Vacuum **114**, 131 (2015).
[7]J. Vlček, A. Belosludtsev, J. Rezek, J. Houška, J. Čapek, R. Čerstvý, and S. Haviar, Surf. Coat. Technol. **290**, 58 (2016).
[8]A. D. Pajdarová, J. Vlček, and J. Rezek, J. Appl. Phys. **121**, 171908 (2017).
[9]N.-W. Pi, M. Zhang, J. Jiang, A. Belosludtsev, J. Vlček, J. Houška, and E. I. Meletis, Thin Solid Films **619**, 239 (2016).
[10]T. Kozák and J. Vlček, J. Phys. D: Appl. Phys. **49**, 055202 (2016).
[11]S. M. Rossnagel, J. Vac. Sci. Technol. A **6**, 19 (1988).
[12]H. Park and W. Choe, Curr. Appl. Phys. **10**, 1456 (2010).
[13]H. Park, S. J. You, and W. Choe, Phys. Plasmas **17**, 103501 (2010).
[14]T. H. Chung, H. Ra Kang, and M. K. Bae, Phys. Plasmas **19**, 113502 (2012).
[15]D. M. Devia, L. V. Rodriguez-Restrepo, and E. Restrepo-Parra, Ing. Cienc. **11**, 239 (2015).
[16]Ü. Aydin, P. Roth, C. D. Gehlen, and R. Noll, Spectrochim. Acta B **63**, 1060 (2008).
[17]N. U. Rehman, M. Zakaullah, F. U. Khan, and S. Naseer, J. Appl. Phys. **104**, 123304 (2008).
[18]D. Depla, S. Heirwegh, S. Mahieu, J. Haemers, and R. De Gryse, J. Appl. Phys. **101**, 013301 (2007).
[19]Y. Yamauchi and R. Shimizu, Jpn. J. Appl. Phys. **22**, L227 (1983).
[20]M. Aiempanakit, A. Aijaz, D. Lundin, U. Helmersson, and T. Kubart, J. Appl. Phys. **113**, 133302 (2013).
[21]F. Magnus, T. K. Tryggvason, S. Olafsson, and J. T. Gudmundsson, J. Vac. Sci. Technol. A **30**, 050601 (2012).
[22]R. Ganesan, B. Akhavan, J. G. Partridge, D. G. McCulloch, D. R. McKenzie, and M. M. M. Bilek, J. Appl. Phys. **121**, 171909 (2017).
[23]T. Kozák and J. Vlček, J. Appl. Phys. **122**, 043304 (2017).
[24]A. D. Pajdarová, J. Vlček, P. Kudláček, and J. Lukáš, Plasma Sources Sci. Technol. **18**, 025008 (2009).
[25]P. Poolcharuansin and J. W. Bradley, Plasma Sources Sci. Technol. **19**, 025010 (2010).
[26]A. Anders, P. Ni, and A. Rauch, J. Appl. Phys. **111**, 053304 (2012).
[27]A. Hecimovic, C. Corbella, C. Maszl, W. Breilmann, and A. von Keudell, J. Appl. Phys. **121**, 171915 (2017).
[28]C. Maszl, W. Breilmann, J. Benedikt, and A. von Keudell, J. Phys. D: Appl. Phys. **47**, 224002 (2014).
[29]M. Panjan, R. Franz, and A. Anders, Plasma Sources Sci. Technol. **23**, 025007 (2014).
[30]N. Brenning, D. Lundin, T. Minea, C. Costin, and C. Vitelaru, J. Phys. D: Appl. Phys. **46**, 084005 (2013).
[31]M. Panjan and A. Anders, J. Appl. Phys. **121**, 063302 (2017).
[32]V. Straňák, Z. Hubička, P. Adámek, J. Blažek, M. Tichý, P. Špatenka, R. Hippler, and S. Wrehde, Surf. Coat. Technol. **201**, 2512 (2006).
[33]M. Čada, D. Lundin, and Z. Hubička, J. Appl. Phys. **121**, 171913 (2017).
[34]W. Trennepohl, Jr, J. Bretagne, G. Gousset, D. Pagnon, and M. Touzeau, Plasma Sources Sci. Technol. **5**, 607 (1996).
[35]H. Kakati, A. R. Pal, H. Bailung, and J. Chutia, J. Appl. Phys. **101**, 083304 (2007).
[36]T. Kozák and A. D. Pajdarová, J. Appl. Phys. **110**, 103303 (2011).
[37]J. Vlček, A. D. Pajdarová, and J. Musil, Contrib. Plasma Phys. **44**, 426 (2004).
[38]C. Vitelaru, D. Lundin, G. D. Stancu, N. Brenning, J. Bretagne, and T. Minea," Plasma Sources Sci. Technol. **21**, 025010 (2012).
[39]C. Huo, M. A. Raadu, D. Lundin, J. T. Gudmundsson, A. Anders, and N. Brenning, Plasma Sources Sci. Technol. **21**, 045004 (2012).
[40]J. Lazar, J. Vlček, and J. Rezek, J. Appl. Phys. **108**, 063307 (2010).
[41]M. A. Lieberman and A. J. Lichtenberg, *Principles of Plasma Discharges and Materials Processing*, 2nd ed. (Wiley, New York, 2005), pp. 243–244, 270, 278–279, 563.
[42]D. Lundin, J. T. Gudmundsson, N. Brenning, M. A. Raadu, and T. M. Minea, J. Appl. Phys. **121**, 171917 (2017).
[43]A. Bogaerts, Spectrochim. Acta B **64**, 1266 (2009).
[44]Y. Itikawa, J. Phys. Chem. Ref. Data **38**, 1 (2009).
[45]A. A. Ionin, I. V. Kochetov, A. P. Napartovich, and N. N. Yuryshev, J. Phys. D: Appl. Phys. **40**, R25 (2007).
[46]J. Vlček and K. Burcalová, Plasma Sources Sci. Technol. **19**, 065010 (2010).